Reedy and Reedy *Heritage Science* (2022) 10:83
https://doi.org/10.1186/s40494-022-00723-4

Heritage Science

RESEARCH ARTICLE Open Access

High-resolution micro-CT with 3D image analysis for porosity characterization of historic bricks

Chandra L. Reedy[1*] and Cara L. Reedy[2]

Abstract

The study of pores in historic bricks is important for characterizing and comparing brick materials, evaluating the degree of deterioration, predicting behavior in future weathering conditions, studying the effectiveness of protective measures, and analyzing the potential effects of cleaning treatments. High-resolution micro-CT coupled with 3D image analysis is a promising new approach for studying porosity and pore systems in bricks. In this technique, hundreds or even thousands of X-ray projection images are acquired at 360 degrees around a sample. The X-radiation passing through the sample is absorbed, with radiation attenuated to varying degrees depending on the varying densities of phases within the object. The 3D volume is reconstructed by a computer algorithm, producing images where each voxel has a grayscale intensity value associated with the component it represents. Recent new instrument designs allow fast scanning with good spatial resolution. In this research, we present a set of protocols for creating optimal images of brick pores in micro-CT scans and for conducting 3D image analysis to extract both qualitative and quantitative data from those scans. Small samples give better spatial resolution for imaging of pores, so given the typical heterogeneity of bricks, scanning multiple samples from each brick ensures that the results are more likely to be representative. Machine learning and deep learning with convolutional neural networks were found to be important tools for better distinguishing pores from the surrounding matrix in the segmentation process, especially at the very limits of spatial resolution. Statistical analyses revealed which of the many parameters that can be measured are potentially most significant for characterizing the pore systems of bricks. These significant pore variables came from a multi-staged image analysis approach and include the total volume percent occupied by pores, the percentage of those pores accessible to the surface versus isolated interior ones, a variety of statistical properties of individual pores related to their size and shape, the average number of connections that pores have to other pores, and the length, diameter, and directness of those connections.

Keywords: Micro-CT, 3D image analysis, Porosity, Pore systems, Historic bricks, Ceramic materials, Machine learning, Deep learning, Heritage

*Correspondence: clreedy@udel.edu

[1] Center for Historic Architecture and Design, University of Delaware, 240 Academy Street, 331 Alison Hall, Newark, DE 19716, USA
Full list of author information is available at the end of the article

Springer Open

© The Author(s) 2022. **Open Access** This article is licensed under a Creative Commons Attribution 4.0 International License, which permits use, sharing, adaptation, distribution and reproduction in any medium or format, as long as you give appropriate credit to the original author(s) and the source, provide a link to the Creative Commons licence, and indicate if changes were made. The images or other third party material in this article are included in the article's Creative Commons licence, unless indicated otherwise in a credit line to the material. If material is not included in the article's Creative Commons licence and your intended use is not permitted by statutory regulation or exceeds the permitted use, you will need to obtain permission directly from the copyright holder. To view a copy of this licence, visit http://creativecommons.org/licenses/by/4.0/. The Creative Commons Public Domain Dedication waiver (http://creativecommons.org/publicdomain/zero/1.0/) applies to the data made available in this article, unless otherwise stated in a credit line to the data.

Graphical Abstract

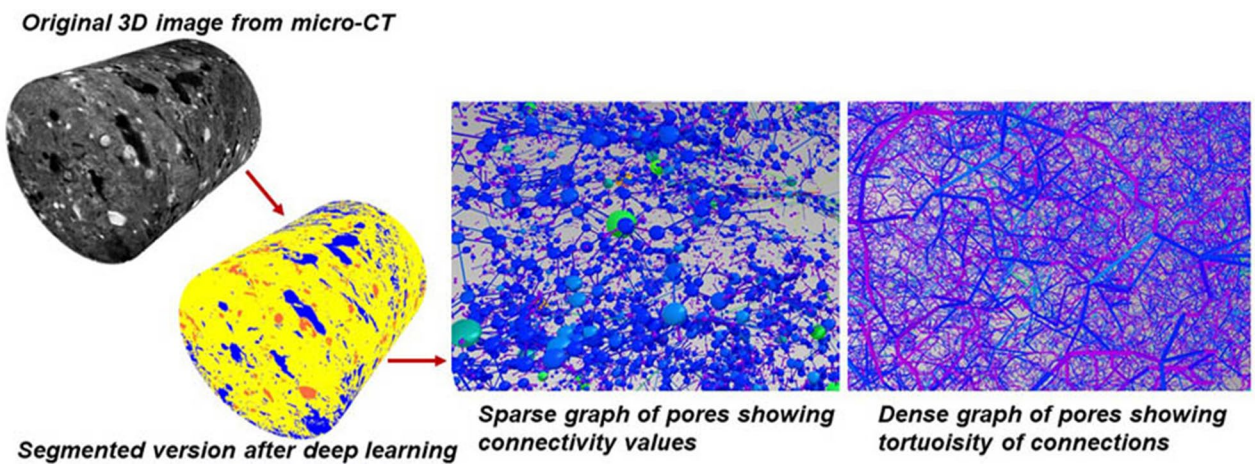

Introduction

Characterizing porosity in historic bricks is important for interpreting and comparing brick materials, evaluating the degree of deterioration, predicting behavior in future weathering conditions, studying the effectiveness of protective measures, and analyzing the potential effects of cleaning treatments. High-resolution micro-CT coupled with 3D image analysis is a promising new approach for studying porosity and pore systems in bricks. The research presented here has the primary goal of using micro-CT scanning and 3D image analysis to identify significant parameters for characterizing brick porosity. Its purpose is to expand the toolkit available to conservation scientists for investigating porosity variables, given how crucial porosity is for interpreting the history and preservation state of historic bricks.

Porosity refers to the volume fraction of a material that is empty space, or voids; the amount and characteristics of that pore fraction in bricks impact the mechanical performance of brick as a building material. Characterizing a brick's porosity reveals information about its raw materials and production technology, use properties, and deterioration susceptibility and mechanisms. While many analytical methods have been used to study porosity, no one method has been found adequate, in part because the void space can span an enormous range in scale [1]. Experiments using micro-computed tomography (micro-CT) to study porosity in ceramics, bricks, or other architectural materials have been conducted for more than 15 years. Most often these experiments compared micro-CT to one or more other techniques for measuring porosity [2–12]. A frequent conclusion has been that porosity values can vary considerably depending on the technique used because each technique works in a somewhat different way and is measuring somewhat different characteristics, types of pores, and pore size ranges. Each technique has advantages and disadvantages.

Previous published applications of micro-CT analysis to brick porosity studies

As an example of the many published comparisons of micro-CT to other porosity analysis techniques, Coletti et al. [13] analyzed the porosity of one sample each from four industrial bricks of differing compositions and firing temperatures by using micro-CT with 3D image analysis. They compared the results to three other methods for characterizing porosity, focusing on total porosity and pore size ranges. They concluded that a porosity characterization benefits from using a variety of methods as each has limitations and no one method can completely characterize the entire pore system and its range of pore sizes. Bugani et al. [14] found that it was difficult to compare results between mercury intrusion porosimetry (MIP) and micro-CT for the pore size range that could be characterized by micro-CT (~ 10 µm and above), which they attributed to the fact the two techniques are based on different physical principles. Importantly, while MIP provides quantitative data, it cannot provide visual data regarding the location or distribution of pores.

Rather than performing yet another multi-technique comparison to micro-CT, this work seeks to highlight where micro-CT coupled with 3D image analysis has strengths that may be useful in characterizing the pore fraction of historic bricks. Some of the limitations of this approach are also highlighted, to emphasize where and when it needs to be augmented by other methods.

Importance of characterizing porosity in bricks

The study of porosity in bricks is important because porosity reflects the choices that were made in raw materials and technology, and because porosity is also strongly connected to a variety of physical and mechanical properties that influence the resilience of a brick structure [15]. Porosity refers to the volume of empty space within a material in the form of voids, or pores, along with cracks that have formed. A pore system consists of a group of pores, many with connections (pore throats) to other pores and/or open to the surface [16].

Porosity in brick results primarily from two technological choices. First, there is the choice of raw materials. If there is a significant fraction of non-clay particles present (whether naturally occurring with the raw material or added to improve drying and firing properties by providing more avenues for release of water) porosity can increase since clay tends to shrink away from those particles during drying and firing; this is especially true for large particles [17–21]. Second, production techniques can heavily influence the pore system. Fabrication methods and firing temperatures and atmospheres can influence the size, shape, and orientation of pores [22, 23]. During firing, additional porosity can be created if carbonates are present to dissociate and organics to burn out or char, and as other particles undergo thermal expansion. If firing temperatures are high enough, porosity will then decline as sintering and vitrification of the clay matrix occurs; the ratio of isolated closed pores to open connected pores will also increase [7, 23]. Round, secondary pores can be produced by trapped gases as the clay matrix and silica minerals begin to melt, off-gas, and vitrify. If temperatures become too high, the round pores can become bloated and expand in number, indicating overfiring [3, 24]. As the firing temperature rises, sealed (unconnected) porosity increases; pore size distribution also varies with firing temperature. Cracks can form during cooling if there are varied thermal expansion coefficients of different fabric constituents [22], which is more noticeable in heterogeneous handmade objects with a high percentage of varied additives. These cracks provide another avenue for pressure-induced water entry.

The connected pores provide a passageway for water to enter and move through the brick by capillary action or by pressure; the flow capacity and how freeze-thaw cycles affect bricks are also controlled by the size, shape, and number of pore throats per pore [25]. Very large pores (> a few mm) are sometimes termed "cavities" and may not contribute to capillary action but can provide ingress for water through pressure (such as wind-driven rain). Small pores (< 5 μm) allow water to enter but not escape easily, causing them to be especially affected by freeze-thaw cycles and enlarge over time. For pores larger than this, water can both enter and escape more freely [26]. Most analyses of pore systems have focused on flow capacity; however, isolated pores (unconnected to other pores or to the surface, or "closed pores") are also important in the study of bricks because they can contribute to other characteristics such as density, mechanical strength, durability, and thermal conductivity [16, 25, 27, 28].

The resulting, often complex, pore system provides an avenue for ingress of water in liquid or vapor form. This is one of the main mechanisms of deterioration through freeze-thaw cyclic damage, salt crystallization damage, transporting of acid and particulate pollution and their reaction products, and disaggregation of the matrix in weakened zones [29]. It has been proposed that it is highly likely that in the future, with more intense and frequent precipitation or flooding events predicted by climate change models, brick structures in some regions will show higher tendencies for moisture-related damage [30].

Porosity in a fired ceramic material such as brick can also be advantageous, so is often deliberate and controlled. Production factors that influence total porosity, pore size distribution, and the type of pores present and their distribution (open and closed, and overall pore morphology) can have a major effect on the physical properties important for bricks such as strength, water absorption, and frost resistance [31, 32]. However, deterioration over time can lead to significant changes in the original pore system, such as an increase in pore size and pore connectivity; pores and throats can become enlarged because of water flow or freeze/thaw cycles and combine with others, and new cracks can form as a result of use and environmental exposure. Understanding the total porosity percentage and the pore structure (size ranges, morphologies, and connectivity) is useful for characterizing the material and comparing it to other similar materials, evaluating the current degree of deterioration, predicting behavior in future weathering conditions, studying the effectiveness of protective treatments, and analyzing the potential effects of cleaning treatments [26, 27, 33, 34].

Micro-CT analysis of bricks

Conventional computed tomography (CT) has been used for decades [35, 36]. In this imaging technique, hundreds or even thousands of X-ray projection images are acquired at 360° of rotation angles around a specimen. X-ray radiation passing through the sample is absorbed, with the radiation weakened to varying degrees depending on the varying densities within the object. The 3D volume is reconstructed by a computer algorithm, producing maps of X-ray attenuation based on the composition/density of the material, with each pixel having an

intensity value associated with the component/phase it represents. Depth information is much better than in 2D radiographs, making the specimen interpretation of 3D images obtained by CT more accurate. This method has been used since its inception in the 1970s as, for example, a medical diagnostic tool to image bone structures [36]. However, such medical CT systems have low spatial resolution, typically hundreds of microns, because of the size of the object being investigated (humans) and the large size of the X-ray source focal spot. Newer high-resolution micro-CT instruments have a much smaller focal spot, with much higher resolution for the internal study of materials (typically 50–100 microns or less in resolution with sample sizes below 5 cm) [37, 38]. Nano-CT can achieve as low as 325 nm spatial resolution but requires small sample sizes (generally 0.5–2 mm) [39].

Synchrotron micro-CT systems have been used for decades, with excellent spatial resolution [40]. However, the difficulty of accessing synchrotron facilities limited the range and quantity of research applications. In recent years, more widely accessible laboratory-based (non-synchrotron) systems have greatly improved with advances in detector technology, more accurate rotation stages, and new acquisition geometries. These laboratory-based systems, often affordable benchtop instruments, are now widely available and can achieve good spatial resolution and high-speed scanning [14], leading to micro-CT now being regularly used as a research tool in materials and composites science and in geology for the study of rock fractures, internal microstructure, porosity, and phase quantification, replacing or augmenting petrography [38, 41, 42]. This technique has been applied less often to the study of bricks or other ceramic materials, and only rarely with quantitative 3D image analysis. Yet, emerging work in allied disciplines and in industry shows that this technique can give a tremendous amount of information about ceramic properties and technologies.

Du Plessis et al. [43] noted that a past downside of using micro-CT in porosity studies was that it usually required time-consuming scans and custom software, but current laboratory-based micro-CT scanners have relatively fast scan times with immediate image reconstruction. Powerful and comprehensive 3D image analysis packages now exist for analyzing and interpreting those scans, eliminating the need for in-house programming. Some of the software packages commonly used are VGStudio, Avizo, Mimics, ImageJ/Fiji, and Dragonfly.

Issues of micro-CT sample size, representativeness, variability, and replication

Achievable voxel size is limited by the sample size, with smaller samples allowing for finer spatial resolution. This means there is a tradeoff between being able to adequately image smaller pores and the representativeness of samples from heterogeneous materials [10]. With handmade and historic bricks, even a cursory examination of the brick interior and of thin sections taken from different locations within the brick highlights the fact that these materials are often quite heterogeneous. A 1-mm sample can be analyzed on a nano-CT instrument with spatial resolution of 350 nm to examine some of the smallest pores and their locations but will not be representative of the brick as a whole or of larger pores within the pore network system. A sample of 2.5 cm will be much more representative of pore sizes, but quantitative data will be limited to larger pores (with our instrument, 50 µm or larger). Higher-resolution scans also greatly increase file size and increase computational demands on image processing. Porter and Wildenschid [44], for example, found that doubling resolution from 11.8 to 5.9 µm/voxel increased datafile sizes by a factor of 8, yet it provided few new insights regarding porosity (leading them to settle for 13 µm resolution for most of their work).

Du Plessis et al. [43] used micro-CT to study the porosity of a concrete sample. They selected a range of sample sizes and resolutions (from 200 µm spatial resolution with 100 mm fields of view so that very large pores could be characterized, down to a 5 mm field of view with 10 µm spatial resolution to characterize smaller pores). The same sample was scanned at six resolutions; for the finest resolutions, the sample was cut. The finer resolution/smaller fields of view allow for smaller detectable pores, but very large pores could not be fully characterized because they were too large for the field of view. They also compared slow and fast scans. Fast scans at lower resolution were found useful when the objects of interest were the largest pores. However, fast scans result in more noise, making detection of smaller pores more difficult.

Most papers reporting micro-CT scanning on cultural materials appear to analyze only one sample per brick or other object. Several studies that did include replication have shown that porosity values can vary greatly from spot to spot for rocks with high heterogeneity [9] and can also vary considerably across fired bricks [11]. Given the high heterogeneity of most bricks, especially handmade ones, a single sample is unlikely to be representative of the brick material.

Materials

Six different brick types were selected for comparison, including three modern hand-molded bricks and three deteriorated historic bricks. The mineralogy for each was identified by thin-section petrography (described in more detail in the Experimental Methods section

below, under the subsection on ancillary methods). The six brick types (A-F) are as follows:

Brick A. Modern hand-molded, Red Thin Brick from Faceables. These red bricks (Fig. 1A) (20 x 5.5 x 1.3 cm) were made by hand to be used as a brick veneer. In thin section (Fig. 2A), the hematite-rich clay appears very sandy. In addition to quartz (very fine- to coarse-grained with both polycrystalline and undulous quartz), the sand has lesser amounts of plagioclase feldspar, metamorphic lithics, and micas (biotite, muscovite, and sericite). Other components are shale and grog (crushed or ground up brick or fired ceramic fragments).

Brick B. Modern hand-molded sand-struck, Brandywine Brick from Delaware Brick Company. These red bricks (Fig. 1B) (21 x 9.5 x 7.0 cm) were manufactured by Glen-Gery in York, Pennsylvania, a major manufacturing site for bricks distributed throughout the Mid-Atlantic. In thin section (Fig. 2B), there is a range of fine to very coarse grains of quartz, metamorphic lithics, shale, and grog, with smaller feldspars and biotite mica. The hematite-rich matrix contains chunks of hematite and some limonite.

Brick C. Modern hand-molded sand-struck, Barlow Brick from Delaware Brick Company. These red bricks (Fig. 1C) (19.0 x 9 x 5.5 cm) were also manufactured by Glen-Gery in York, Pennsylvania. In thin section (Fig. 2C), the quartz component of the hematite-rich matrix is fine-grained, with small biotite micas and larger chunks of shale, grog, and some metamorphic lithics with polycrystalline and undulous quartz.

Brick D. Dutch-style brick recorded as being from the 1687 "Old Tile House" demolished in 1884 in New Castle, Delaware [45]. These yellow-green bricks (Fig. 1D) (17.5 × 8.0 × 3.25 cm) apparently came from the former Dutch townhouse (there were originally many Dutch settlers in historic New Castle). In thin section (Fig. 2D), they appear poorly sorted, with streaks and chunks of sandy quartz within a silty matrix. Along with abundant quartz, there is plagioclase feldspar, muscovite mica, and chunks of hematite and limonite. Within some of the larger hematite chunks are small pools of silica glass.

Brick E. Red brick from a 1768 Cape Cod house in Dennis, Massachusetts. It was used (Fig. 1E) (18 x 8.75 x 6.5 cm) in the construction of a root cellar. In thin section (Fig. 2E), the hematite-rich matrix (with chunks of hematite and bits of limonite) has quartz ranging from silt-sized to very coarse (including some polycrystalline quartz) along with plagioclase feldspar, clinopyroxenes, metamorphic lithics, shale, and small biotite mica particles.

Brick F. Red brick from the John Evans House, built in 1715, in Chester County, Pennsylvania. These bricks (Fig. 1F) (21 x 10 x 6.5 cm) were used in the construction of a now deteriorating farmhouse and some of the bricks have fingerprints from the makers. Such bricks were often handmade on site, often by untrained labor. Raw materials would have been collected nearby, and firing would be done on-site as well, with relatively crude equipment. Bricks were often stacked together with dried bricks forming the walls of the kiln. Wood fuel could create large variations in temperature among sections

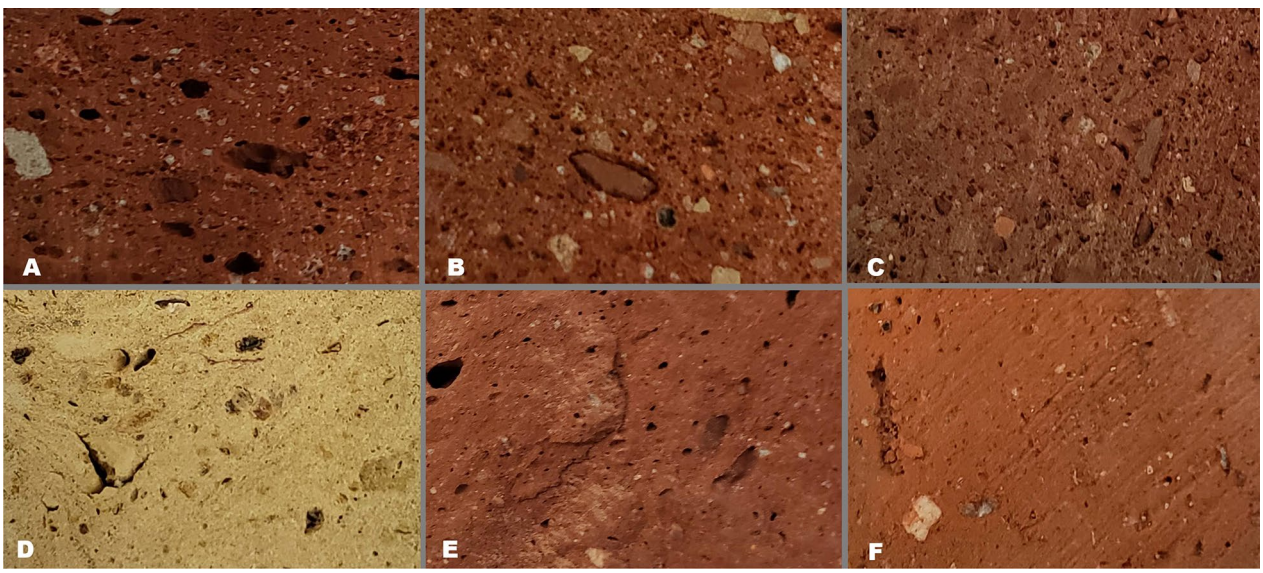

Fig. 1 Cut surfaces of bricks. **A**, **B**, and **C** (top) are three different modern hand-molded bricks. **D** is a yellow-green Dutch-style brick from a 1687 house in New Castle, Delaware. E is from a 1768 house cellar in Dennis, Massachusetts. F is from a 1715 house in Chester County, Pennsylvania

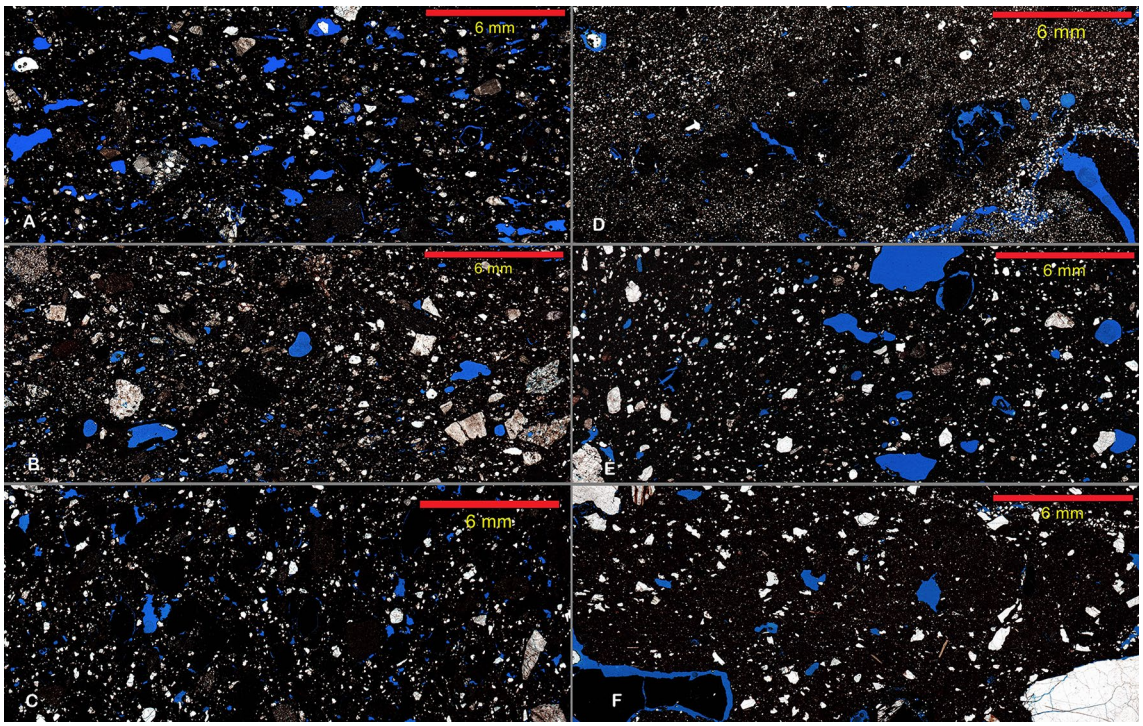

Fig. 2 Thin sections from each brick, mounted in blue-dyed epoxy so pores are blue, then scanned in a Pathscan Enabler 5 geological slide scanner (plane polarized light) at a resolution of 2.54 µm/pixel. Bright particles are silica minerals; fired clay matrix is black. **A**, **B**, and **C** (left) are the three modern hand-molded bricks, and **D**, **E**, and **F** (right) are the three historic bricks seen in Fig. 1

of the kiln [46]. In thin section (Fig. 2F), the material is very inhomogeneous. The hematite-rich matrix contains silt and fine sand-sized grains of quartz along with very coarse chunks of quartz (some polycrystalline), metamorphic lithics, microcline feldspar, micas (biotite, muscovite, and sericite), and chunks of carbonized organic material.

Experimental Methods

HR micro-CT

Most of the experimental work was done on a Rigaku GX130 high-speed high-resolution (HR) micro-CT instrument with cone beam geometry in a shared University of Delaware facility, the Advanced Materials Characterization Laboratory. Samples are placed on a small horizontal holder with a Styrofoam support and centered in the field of view. The sample stays stationary while a micro-focus X-ray source with W target illuminates it (X-ray source to center of rotation 120 mm) and a 7 Mp flat-panel X-ray detector (FPD) circles 360° degrees around it while collecting magnified projection images at view angles uniformly distributed around the object. The FPD detector active area size is 116.424×145.728 mm, with pixel dimensions of 2352×2944 pixels, pixel size 49.5 µm, and distance of FPD to center of rotation is 224 mm. High-speed gantry rotation of the detector enables high-speed data collection. The number of projections needed for good resolution on this instrument is determined by the software according to the field of view to be covered and the voxel size. For our experiments, 803 projections were determined to be necessary for producing quality images that successfully show the features of interest. However, many other experimental parameters contributed to the high quality of the images by reducing signal-to-noise ratio, improving phase contrast, and reducing beam hardening artifacts. To reduce noise in images, the longest supported scan time for this instrument (57 min) was used, with an initial 57-min warm-up. Gain calibration was performed prior to each imaging session to minimize noise and artifacts in the final images by correcting for the non-uniform response of individual pixels of the detector to X-ray exposure. Creating samples only slightly larger in size than the scanned field of view also reduced noise in the images. Phase contrast and image quality were maximized by experimenting with settings such as the focus spot size, source voltage, source intensity, and filter selection to identify the most appropriate choices for the sample type and size. For the brick samples of 0.5 cm^3, using a small focus spot size (5 µm) allowed for higher resolution. The optimal settings for

best contrast were found to be 130 kV and 61 μA. A 0.06 mm Cu and 0.5 mm Al filter combination improved contrast and reduced beam hardening artifacts [14]. The Rigaku software employed to create the 3D reconstruction (in 15 s) using a FBP (filtered back projection) reconstruction algorithm incorporates a ring reduction filter to minimize ring artifacts inherent in CT scans.

This instrument has a nominal resolution (smallest possible voxel size of a reconstructed image) of 4.5 μm. However, the actual spatial resolution (how far apart two features need to be in order to be distinguishable in an image) depends on a variety of experimental choices – smaller samples will give better spatial resolution, and longer scan times will produce less noise and make smaller features more easily visible. The finest spatial resolution that can be obtained with this instrument is 10 μm with a 5 × 5 mm field of view, with sample sizes no more than about twice the size or thickness of the field of view to reduce noise. Confirming what spatial resolution was achieved was done by scanning a micro-CT bar pattern chip phantom from QRM. This is a chip placed in an air-filled cylinder and inscribed with bar and point patterns with diameters ranging from 5 to 150 μm line/point thickness. When scanned under the same experimental protocol as the samples, the image is used to evaluate spatial resolution in the center and periphery of scans. Linewidths and spot sizes of 150, 100, 50, 25, 20, and 15 μm could easily be measured. The 10 μm line or spot widths were at the limits of spatial resolution and could be measured with some effort, and the 5 μm ones were discernible but too blurry to accurately measure.

The reconstructed image can be viewed as a single slice at a time in X, Y, or Z axes (width, height, and depth) or as a 3D image (Fig. 3). One can scroll through all 2D slices in each axis and manipulate the 3D image to view any part of the surface. The grayscale images can be colored by using a variety of alternative lookup tables.

Five 0.5 cm^3 samples (giving 10 μm spatial resolution) from each of the six bricks were analyzed under these parameters and were used for the statistical analyses. These 30 samples were supplemented with experiments on a 1 cm sample (with a spatial resolution of 20 μm), and a 2.5 cm sample (with a spatial resolution of 50 μm) from each brick. In addition, courtesy of Aya Takase at Rigaku, a 0.5 cm-diameter sample from each brick that was first scanned on our instrument was also scanned using a

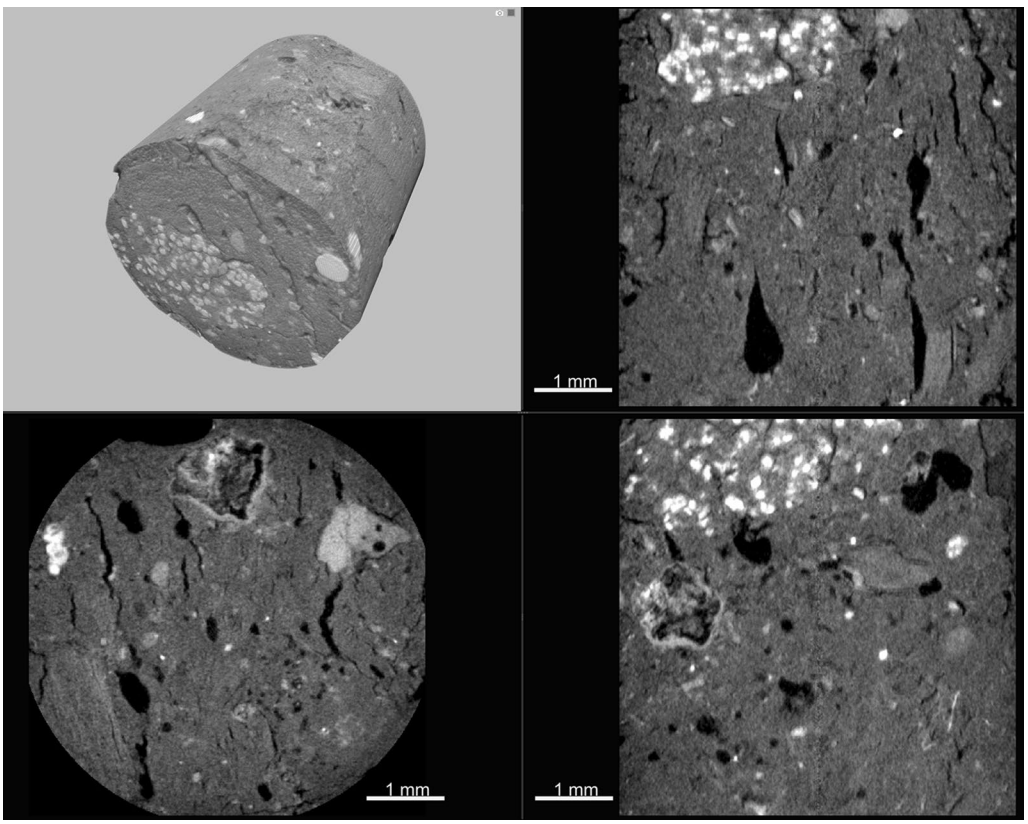

Fig. 3 A micro-CT scan of a brick sample showing single 2D slices in X, Y, and Z axes and the complete reconstructed 3D image in the upper left. Dark areas are the pores, white spots are silica mineral grains, and gray areas are the fired clay matrix

Rigaku CT Laboratory HX130 instrument (parallel beam geometry, with the sample rotating 360° while the X-ray detector is stationary). With a 0.5 cm diameter sample and 5 × 5 mm field of view, it has a resolution of 2.13 µm.

Micro-CT work can be augmented with submicron-resolution scans using instruments such as the Rigaku Nano 3DX CT scanner. Using a parallel beam X-ray geometry, high-flux X-ray source, and optical lens magnification, it can achieve 325 nm resolution, again with relatively fast scanning times. To achieve the best resolution, though, requires very small samples (generally about 1 mm diameter). While this can give information on the tiniest pores, much is lost regarding the representativeness of the material with such small samples for a material like handmade brick, so nano-CT work is not included in this study. Additionally, micro-CT is used to image and measure what are defined in the literature in various ways as macropores [27, 47, 48]. While micropores and mesopores affect some weathering characteristics, additives commonly used to optimize the physical properties of fired bricks and these mixtures, along with the heterogeneity expected of handmade materials, often lead to the presence of many large pore spaces, making micro-CT a good characterization technique to use for bricks [11].

3D image analysis

After careful review of options, we selected the Dragonfly software package (version 2021) by Object Research Systems [49], which is free for academic users and has a wide range of capabilities. After much experimentation, the following multi-stage set of protocols was adopted:

(1) Intensity calibration was first done on each image, calibrating the mean intensity of pores (darkest areas), silica mineral particles (brightest areas), and ceramic matrix (in-between areas) to standard intensities. The main purpose of this step was to bring the set of samples closer in intensity values and hence reduce the number of separate segmentation models needed.
(2) A Region of Interest (ROI) was defined for the sample to eliminate the background area and exclude surface roughness.
(3) A segmentation model was created and applied to separate the pores, particles, and matrix using the "segment with artificial intelligence" tool in Dragonfly. To create a model, one slice was selected, and then initial Otsu thresholding separated the image into classes [50]. This thresholding was edited manually using a paintbrush tool to add or erase phase markings that had been incorrectly marked by the thresholding tool.

Manual editing was aided by comparing the micro-CT image to images of thin sections from the same material, which was especially useful to help discern non-clay particles from the matrix. Comparisons were also made between the original micro-CT scan and enhanced scans that helped to identify boundaries of pores and particles that were at the margins of spatial resolution (Fig. 4). One of these enhanced images was created by applying a set of three filters to the original image (gradient-domain fusion, histogram balance, and a median filter); the second was created using a Noise2Noise regression denoising model, which uses deep learning to clean up noise on the original micro-CT image [51].

Once the image segmentation was satisfactorily edited, a selection of machine learning and deep learning models were trained on that data. Other researchers have found that machine learning approaches improve the reliability and accuracy of segmentation of pores from solids, especially for noisy areas and edges of images, giving a more

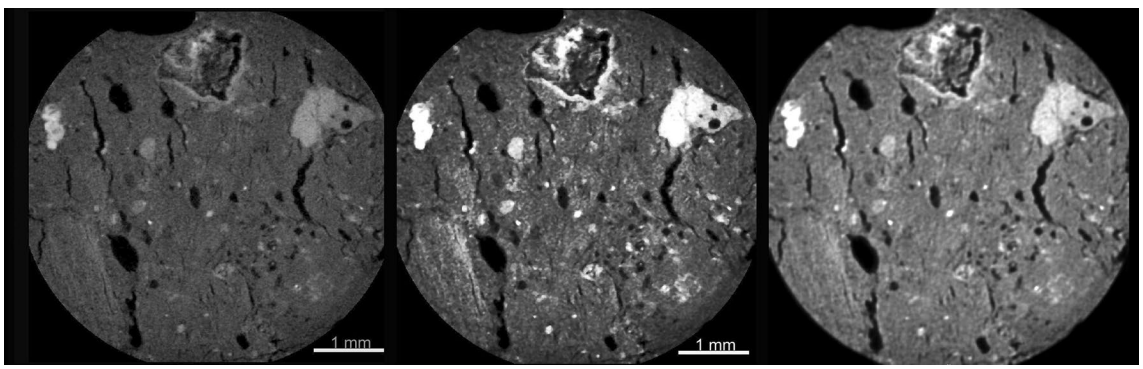

Fig. 4 An original micro-CT scanned brick 2D image (left); the same image after the gradient-domain fusion, histogram balance, and median filters were applied (center); and after applying the Noise2Noise deep learning model (right)

robust classification [52]. After the training was completed, a new slice was used to compare the segmentation predictions of the models, and the model with the best result was promoted for further training, again with manual editing when needed. The process was continued until a model had been refined enough to produce satisfactory segmentation with no further manual editing required (usually 3-5 slices were needed). The trained model was saved and applied simultaneously to all slices in the entire 3D image (Fig. 5). For subsequent samples, the deep learning process only had to be repeated if none of the already-trained models gave good results; the first intensity calibration step meant that one trained model could be applied successfully to many samples in addition to the one on which it was trained.

(4) The pore and particle classes were separately extracted from the segmentation result. Each was then processed to eliminate noise (speckling) and to fill in tiny holes in pores or grains that were simply imaging artifacts. A multi-ROI (multi-Region of Interest) was then created for each (i.e., the voxels were automatically grouped into components based on connectivity). In addition to calculating the volume percentage of pores and particles within each sample, a variety of statistical properties were calculated for individual pores and particles (discussed below). These variables were selected based upon a survey of the literature and variables reported in porosity studies of bricks and other building materials. The initial list of 88 variables recorded for each sample at this stage of image analysis included, for both pores and particles, the minimum, maximum, mean, and standard deviation of pore volume, surface area, volume/surface area, phi, theta, aspect ratio, minimum Feret diameter, mean Feret diameter, maximum Feret diameter, minimum orthogonal Feret diameter, and minimum orthogonal/maximum Feret diameter. Of these initial 88 variables, 16 of them were found to be significant for characterizing bricks given the variability between replicates. These 16 variables are discussed in detail below in the subsection on statistical properties of pore multi-ROIs.

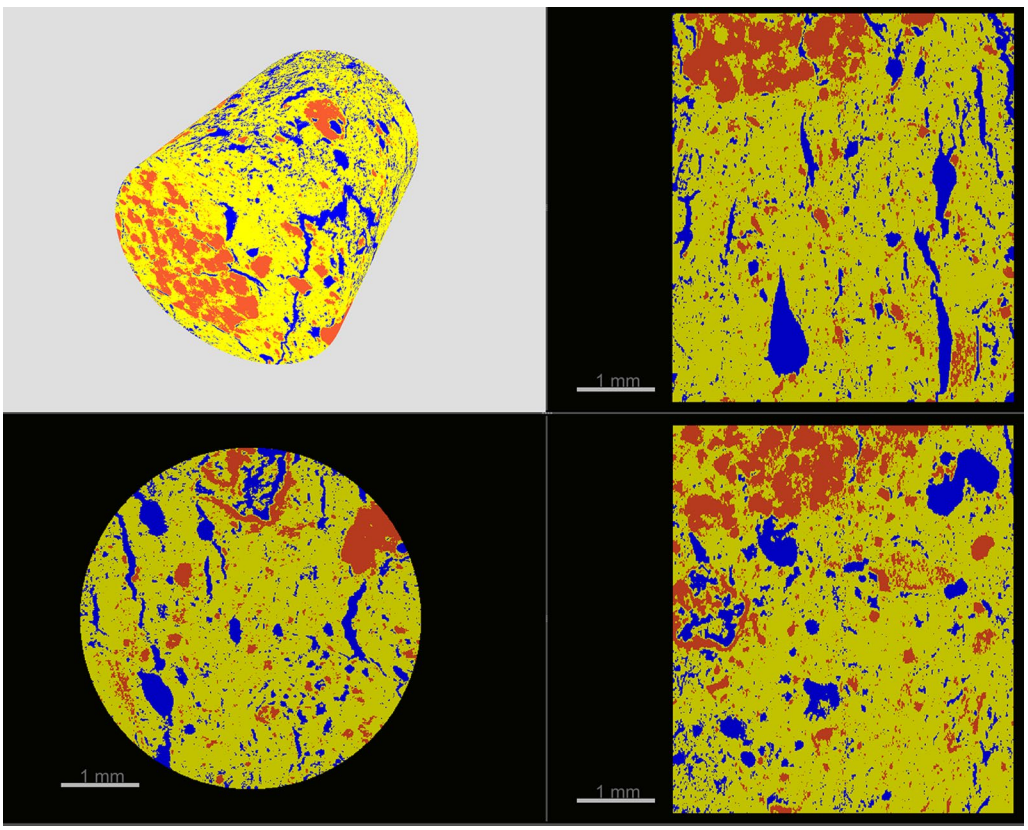

Fig. 5 A final, trained deep learning model was applied to all slices simultaneously to segment pores (blue), silica sand particles (red), and matrix (yellow)

(5) The percentage of pores accessible to a surface versus inaccessible interior ones was calculated by first making a version of the Region of Interest that was just one pixel wide along all edges (a shell). All pores touching a surface in any of the slices were then removed, leaving only inaccessible interior pores, which were marked with one color; then only pores touching the surface shell were considered, and they were marked in another color. The volume percentage of each was then calculated.
(6) Next, a sparse graph of pores was created. This is a model of the pore system with spheres representing pores and lines the connections (pore throats). This was used to collect data on five more variables regarding the connectivity of pores (also called coordination number): the minimum, maximum, mean, and standard deviation of pore connectivity, and the percentage of unconnected pores.
(7) Then a dense graph of pores was created, which shows all individual pixels connecting them. Sixteen variables were collected from this graph; in addition to the same five connectivity values as above, this graph gives better values on the length of connections and includes tortuosity data (a measure of how indirect the connection pathway is). Only ten of these variables were found to be significant for characterizing the brick types, and these are all fully discussed below in the subsection on data from dense graphs of pores.
(8) The final pore data came from a pore network model using OpenPNM, an open-source program [53] available as a plug-in within Dragonfly. In a pore network model, a simplified form of the network of connected pores and throats is used to simulate transport in porous materials and to predict capillary-controlled multi-phase flow and absolute permeability [54]. The model also provides data such as tortuosity, length of throats, and connectivity, which are significant factors in flow modeling [53]. We recorded the total number of vertices (pores), the number of edges (connections), and the ratio of number of connections/number of pores, as well as the maximum, mean, and standard deviation for connectivity of pores in a sample. An additional 21 variables were recorded for aspects of pore and connection diameter, equivalent diameter, direct length, and volume.
(9) Finally, a sparse graph was created for the particles, with each particle a node and the number of particles that touch each other representing connectivity. This gives information about the packing of grains. While our research focused on characterizing porosity and pore systems, the amount of porosity and the size, morphology, and structure of pore systems are sometimes strongly dependent on the natural and added particles present [11]. For example, using pore network modeling to study micro-CT images after segmentation, Thomson et al. [55] studied the geometry of pore networks in two different sandstones. They found that the networks consisted of pores situated at the corner of sand grains (and the junction of grain-to-grain contacts), and elongated pore throats were located along grain edges. We visually examined the relationships of grains and pores.

Statistical analyses

Statistical analyses of all 148 pore variables collected during image analysis of each of the 30 0.5 cm^3 samples had the primary purpose of identifying which of the many recorded variables are useful to characterize a brick type and to distinguish it from other brick types, given the heterogeneity of the bricks and the range of variability in porosity from one sample to another within each brick. All statistics were done in Python 3 with the Pandas package for data handling, SciPy package for analysis of variance (ANOVA), and scikit-learn package for linear and quadratic discriminant analysis. The Matplotlib package was used for plots.

The data were first checked for any variables that were identical across all samples; these were removed from any further data analysis. A one-way ANOVA was then used to identify any variables that might be significant for characterizing a brick type across all replicates (at $p < 0.05$). A correlation matrix identified which variables were highly correlated with each other. Finally, the significant values were used in a stepwise linear and then quadratic discriminant analysis checked with repeated stratified k-folds, to see which combination of variables best discriminates between all six brick types.

Ancillary methods

Thin-section petrography

Three samples (2.5 × 4.5 cm) from each brick were taken for thin-section petrography. The thin sections were prepared and mounted on glass slides with blue-dyed epoxy (so pores could be readily distinguished) by Spectrum Petrographics [56]. One thin section was polished and uncovered for examination of opaque metal oxides; two were given coverslips. Originally, we planned to use 2D image analysis of porosity in thin sections as a comparison to micro-CT results [24, 57, 58]. However, it quickly became apparent that since such images only show a single 2D slice through the material, they were simply not

very comparative to images of the 3D pore networks or to connectivity within those networks that micro-CT images provide [4] (2D image analysis using the same Dragonfly software gave pore area percentages that were always significantly lower than results obtained with 3D image analysis of micro-CT scans).

A major advantage of thin sections, however, is that producing them permits identification of the particles present. This proved to be useful in the segmentation of particles in micro-CT images. Interpreting the grey-scale densities of minerals, lithics, and other particles and separating them from a ceramic matrix is much easier when the micro-CT scan can be displayed next to a petrographic thin section, especially when particles are similar in density to the matrix. Most useful was an entire thin section scanned at low magnification using a Pathscan Enabler 5 geological slide scanner, at a resolution of 2.54 µm/pixel (10,000 × 10,000 dpi). This scan was displayed on one monitor while components in micro-CT images were being segmented for deep learning in Dragonfly on the other monitor. When necessary, minerals, lithics, or other thin section particles were examined more closely in images captured at higher magnification using a Nikon Eclipse 50i POL microscope system.

Accelerated weathering of samples

One advantage of micro-CT is that since it is non-destructive, the same sample can be imaged before and after accelerated aging and/or treatment applications to understand what internal changes the brick may have gone through [38, 41, 42, 59]. After the initial micro-CT scanning work was completed, we selected one of each of the modern handmade brick 0.5 cm^3 samples for accelerated weathering followed by re-scanning the samples with the same field of view as before to see if any changes in porosity could be observed. The accelerated weathering was done in a QUV weatherometer for 1000 h, continuously cycling 8 h of UV exposure at 70°C with 4 h of condensation at 50°C. Changes in volume percentage porosity and porosity accessible to the surface due to the weathering were recorded.

Results and discussion

It was apparent during the image analysis that hand-molded and historic bricks are very heterogeneous materials, and analysis of the data confirmed that impression. Coupled with the fact that the best spatial resolution with micro-CT requires relatively small samples, clearly replication is important. It is therefore concerning that most papers reporting micro-CT on bricks and other cultural materials appear to analyze only one sample per object. It proved to be important that five replicates from each brick were analyzed, so that variation between samples from an individual brick could be taken into account in identifying which variables might work best to characterize a brick and distinguish it from other brick types.

Of the 148 variables recorded, 41 variables related to pores proved to be significant for characterizing brick types at the $p < 0.05$ level. For 20 out of the 41 variables, the Shapiro-Wilks test for normality had p values of < 0, indicating that the distribution may be non-normal. However, because this is an initial screening experiment intended to explore what variables might be significant for differentiating between non-randomly selected brick types in the face of within-brick variability, we did not feel the need to explore possible data transformations.

For particles, 17 variables were found to be significant in distinguishing brick types. These included the particle volume percentage and standard deviation, and two variables from the sparse graph of particles (connectivity mean and standard deviation). Connectivity with regard to particles provides information about the packing of grains, which is related to production methods and affects use functions. The other 13 significant particle variables relate to various size and morphology characteristics and distributions identified in the particles multi-ROI. Since this paper focuses on the work with pores, the particle variables are not discussed further here; however, these results do indicate that the micro-CT technique is sensitive enough to be able to identify potentially significant data about non-clay particles within a ceramic matrix, so this will be one area of concentrated future experimentation.

The 41 significant variables are discussed in the five sections below: porosity percentages; statistical properties of pore multi-ROIs; connectivity data from the sparse graphs of pores; data from the dense graphs of pores; and data from pore network modeling using OpenPNM. Following the main results for the 41 pore variables below, some additional statistical analyses are briefly discussed.

Porosity percentages (volume fraction)

The volume percentage (volume fraction) of pores in each sample was calculated by comparing the region occupied by pores with the entire segmented region of interest. This proved to be a significant variable; Table 1 shows the mean volume percent pores for each brick type. Brick F stands out with the highest mean value. As described in step (5) of the 3D image analysis section above, the percentage of pores accessible to the surface versus inaccessible interior pores was calculated, and both the percentage accessible to the surface and the ratio of surface-accessible to the inaccessible interior pores were found to be significant. The means for these variables for each brick type are also given in Table 1, where again brick F stands out with the highest values.

Table 1 Mean volume percentage of pores in each brick type, mean pores accessible to the surface, and mean ratio of the surface-accessible pores to inaccessible interior pores (n = 5 for each brick type)

Brick	Pore vol. %	Percent accessible to surface	Ratio of the surface accessible/inaccessible interior pores
A	18.5	15.9	9.0
B	23.7	22.4	31.8
C	16.9	14.9	7.6
D	21.0	18.2	18.6
E	21.0	18.9	10.5
F	36.8	36.1	65.8

Figure 6 illustrates these differences. Table 2 shows the importance of replication. For all brick types, there is variation due to inhomogeneity of bricks where porosity varies as a result of varying size, composition, or clustering of additives; or due to fabrication methods, uneven firing temperatures, or uneven deterioration. Clearly, a single micro-CT analysis might be misleading; the more samples that can be analyzed, the better the group means will capture the inherent variation.

Statistical properties of pore multi-ROIs

The 16 variables from an analysis of the statistical properties of the connected components in the pore multi-ROIs that were found to be significant include:

- Maximum pore volume;
- Maximum and standard deviation of pore surface area (interpolated) (i.e., outside area of the pores);
- Mean and standard deviation of volume-to-surface area (interpolated) ratio;
- Mean and standard deviation of aspect ratio (a perfect cube or sphere has an aspect ratio of 1.0, a square or circle 0.5, and a perfect rod of one voxel wide or a point is 0.0);
- Standard deviation of minimum Feret diameter (minimum caliper diameter, or shortest distance between any two points along each pore's boundary), mean and standard deviation of mean Feret diam-

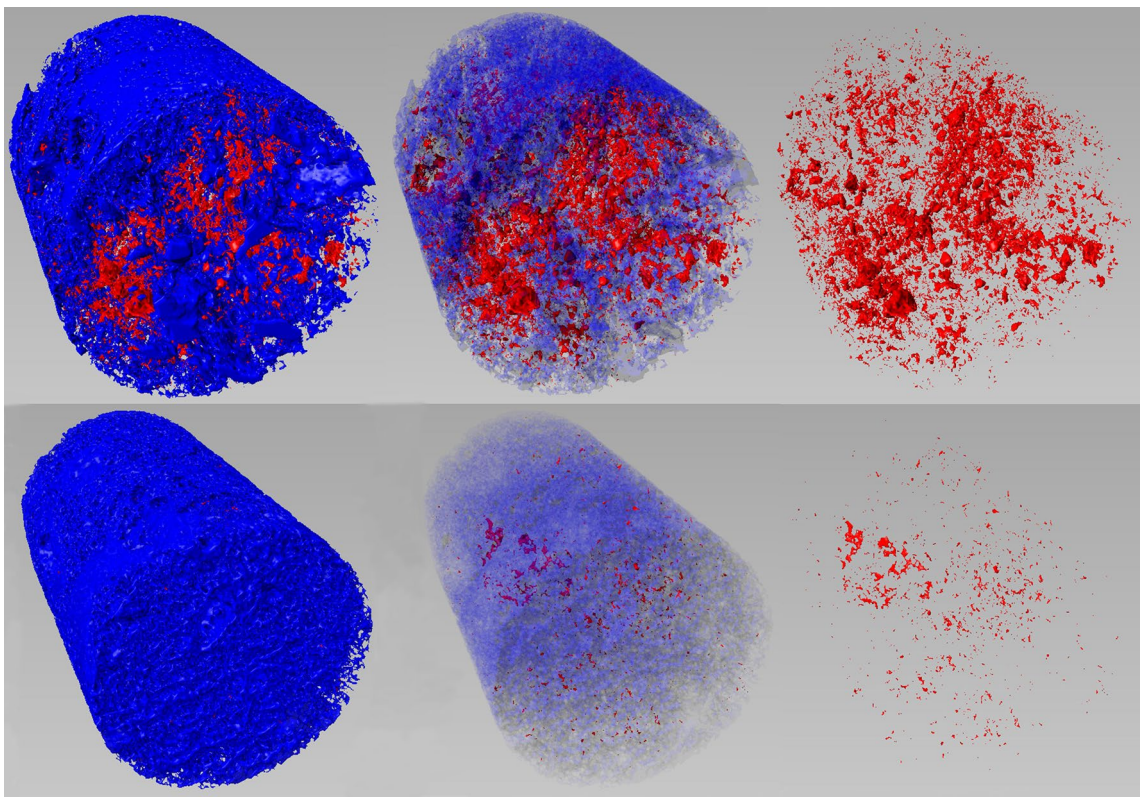

Fig. 6 A sample from brick A (top row) with 17.8% pores, 15.5% of them accessible to the surface (blue) with a surface/interior pore ratio of 6.7. Pores not accessible to the surface are in red. In the center images, surface-accessible pores are made partially transparent so interior ones are more visible; on the right, only the interior pores are shown (2.3%). The bottom row shows a sample from Brick F with 32.8% pores, 32.4% of which are accessible to the surface, leaving only 0.4 vol.% as interior pores inaccessible to the surface (surface/interior ratio of 81)

Table 2 Total volume percentage of pores, percent accessible to the surface, and ratio of surface-accessible to interior pores

Brick	Pore vol. %	Percent accessible to surface	Ratio of the surface accessible/inaccessible interior pores
A	14.1	12.1	6.1
A	23.4	21.6	12.0
A	10.8	4.8	0.8
A	26.6	25.3	19.5
A	17.8	15.5	6.7
B	29.4	28.8	48.0
B	27.8	27.2	45.3
B	11.0	7.9	2.5
B	22.9	22.4	44.8
B	27.2	25.8	18.4
C	16.7	14.9	8.3
C	18.5	16.9	10.6
C	17.5	15.6	8.2
C	16.3	14.2	6.8
C	15.7	12.7	4.2
D	11.3	6.2	1.2
D	21.2	19.1	9.1
D	37.3	36.8	73.6
D	18.8	15.7	5.1
D	16.3	13.1	4.1
E	8.3	5.5	2.0
E	27.1	25.7	18.4
E	23.6	20.9	7.7
E	22.2	20.1	9.6
E	23.7	22.2	14.8
F	32.8	32.4	81
F	37.2	36.7	73.4
F	34.2	32.5	19.1
F	46.0	45.6	114.0
F	34.0	33.2	41.5

eter (mean value of the minimum and maximum Feret diameters of each pore's boundary); and mean and standard deviation of maximum Feret diameter (longest distance between any two points along a pore's boundary, or maximum caliper diameter);

- Mean and standard deviation of the minimum orthogonal Feret diameter (shortest distance between any two points along each pore's boundary that are orthogonal to the pore's maximum Feret diameter); and
- Mean and standard deviation of the minimum orthogonal/maximum Feret diameter (ratio of the minimum orthogonal Feret diameter to the maximum Feret diameter, which can provide a good indication of the elongation of a pore).

As Table 3 shows, Brick F again stands out, having either the lowest (in italics) or highest (in bold) means for all but one of these variables. Figure 7 illustrates one example, contrasting samples from Brick A and from Brick F with a variable that indicates pore elongation (the ratio of the minimum orthogonal to the maximum Feret diameter).

Connectivity data from sparse graphs of pores

Table 4 shows the means for each brick type for the four significant connectivity (number of pores with which a given pore shares throat/connection voxels) variables obtained from sparse graphs of pores. Bricks E and F have noticeably higher maximum connectivity, with F having the highest; the same is true for the mean connectivity and the standard deviation. The reverse is true for the percentage of unconnected pores (Bricks E and F are the lowest, with F considerably lower). Figure 8 contrasts a sample from group A (with 10.8 vol.% pores), which has a maximum connectivity of 15, mean connectivity of 1.67, and 6% of pores unconnected (isolated) with a sample from group F (32.8 vol.% pores) which has a maximum connectivity of 46, mean connectivity of 3.89, and no unconnected pores. Spheres (pores) are sized and color-coded by number of connections (from low to high: purple, dark blue, light blue, green, yellow, orange, red), while the rods indicating connections are sized and color-coded by length.

Data from dense graphs of pores

Ten variables recorded from the dense graphs of pores were significant (Table 5). The connectivity variables again show bricks E and F with much higher pore connectivity than the other bricks. Tortuosity variables characterize the convoluted pathways of connections as a ratio of the length of a straight-line distance between two pores versus the geometric complexity present. The three historic bricks (D, E, and F) tend to have lower values for tortuosity than do the modern hand-molded bricks. Figure 9 compares a sample from Brick A with higher throat tortuosity to a sample from brick F that has a lower tortuosity. Table 5 also shows that the pore connections in the three historic bricks (D, E, and F) have lower mean values for segment Euclidean lengths than do the three modern hand-molded bricks. This refers to the line length of the segments connecting two branches (throats) or connecting a branch with an end node (pore); one exception is the mean edge segment Euclidean length standard deviation for Brick C.

Data from pore network modeling with OpenPNM

The last eight variables are from the pore network modeling step using the OpenPNM program available within

Table 3 Significant ($p < .05$) variables from analysis of the statistical properties of the pore multi-ROIs

Measured variables	Brick A	Brick B	Brick C	Brick D	Brick E	Brick F
Vol. max μm^3	1.20E+10	1.28E+10	*0.93E+10*	1.04E+10	1.46E+10	**2.33E+10**
Surface area (interp.) max μm^2	7.28E+08	7.33E+08	*6.11E+08*	8.17E+08	11.3E+08	**16.8E+08**
Surface area (interp.) SD μm^2	*2.69E+04*	3.88E+04	2.80E+04	3.00E+04	3.61E+04	**6.12E+04**
Vol./sur area (interp.) mean µm	3.31	**3.32**	3.24	3.18	3.06	*2.62*
Vol./sur area (interp.) SD µm	**1.79**	1.77	1.76	1.44	1.30	*0.90*
Aspect ratio mean	**0.168**	0.164	0.160	0.160	0.154	*0.096*
Aspect ratio SD	0.200	**0.202**	**0.202**	0.198	0.192	*0.168*
Min Feret diameter SD µm	27.3	**31.0**	29.0	25.2	22.3	*18.4*
Mean Feret diameter mean µm	**36.7**	35.6	34.6	34.8	32.9	*24.6*
Mean Feret diameter SD µm	45.7	**51.3**	45.4	40.6	35.3	*28.5*
Max Feret diameter mean µm	**45.2**	43.3	42.2	42.3	39.8	*29.5*
Max Feret diameter SD µm	59.2	**61.7**	56.0	49.9	43.1	*33.7*
Min ortho Feret diameter mean µm	**25.1**	24.9	24.3	24.4	22.6	*18.5*
Min ortho Feret diameter SD µm	28.5	**32.0**	29.6	25.9	23.1	*19.1*
Min ortho/max Feret diameter mean µm	*0.650*	0.664	0.664	0.666	0.656	**0.702**
Min ortho/max Feret diameter SD µm	**0.152**	0.148	0.150	0.144	0.148	*0.138*

The lowest value of the means for each variable is in *italics*; the highest value is in **bold**. Brick data = mean of 5)

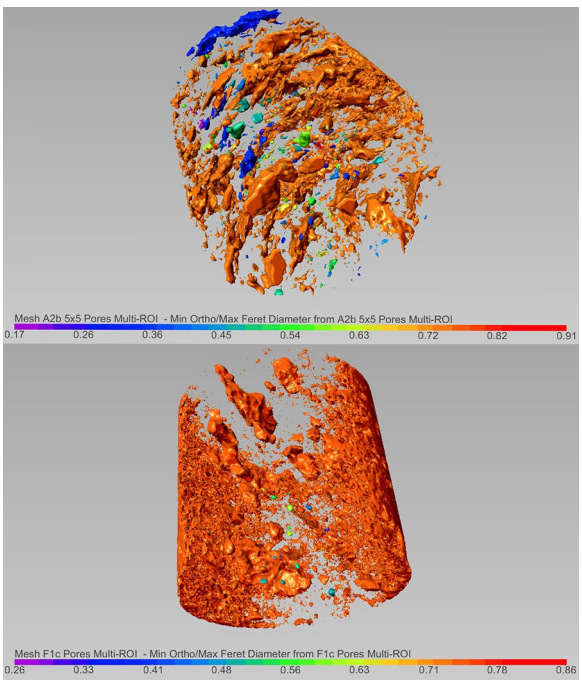

Fig. 7 The (mesh) pore multi-ROI from a sample from group A (top) and group F (bottom), color-coded by minimum orthogonal/maximum Feret diameter ratio indicating pore elongation. Both have pores mainly near the high end of the scale (orange). However, the sample from Brick A has a significant number of pores ranging from orange down to the lower colors of the scale (yellow, green, blue, and purple). The one from Brick F has only a few small pores in the yellow, green, and blue range, and none are purple

Dragonfly. The number of vertices and connections, the ratio of number of throats/number of pores, edge direct length mean and standard deviation, edge equivalent diameter mean, and vertex equivalent diameter mean and standard deviation were all significant at $p < 0.05$. The means for the five samples in each group (Table 6) show much variation among the brick types, with brick F again especially standing out. Figure 10 compares a pore network model of a sample from brick A with one from brick F. The size of the pores in F are often larger than in A (equivalent diameter mean 303 µm for F versus 230 µm for A) and its throats/connections are longer and larger (direct length mean of 862 µm for F versus 398 µm for A, and equivalent diameter mean 180 µm for F versus 119 µm for A). In Fig. 10, the connections are color coded by direct length. We can see that the pore network in the sample from brick A has many shorter connections (purple and dark blue) along with a few longer ones (light blue, green, and yellow). In contrast, the sample from F shows fewer connections in purple and dark blue and more in light blue, green, and yellow, and even a few that are orange and red (highest end of the scale).

Any of the graphs or modeling methods used for pores can be applied to the particles within a brick as well, with each particle as a node and the number of particles that touch each other representing connectivity. This gives information about the packing of grains, which can be affected by production methods and can in turn affect the material properties of a brick. In Fig. 11 the pore network model from OpenPNM is superimposed with the particle network model, to examine the relationship of particles

Table 4 Significant ($p < .05$) connectivity data from the sparse graphs of pores (Brick data = mean of 5)

Measured Variables	Brick A	Brick B	Brick C	Brick D	Brick E	Brick F
Pore connectivity maximum	22.4	22.2	22.6	23.0	31.8	38.2
Pore connectivity mean	2.29	2.55	2.47	2.55	2.71	3.49
Pore connectivity SD	1.58	1.58	1.71	1.71	1.94	2.18
Percentage unconnected pores	3.0	2.8	2.8	2.8	2.4	0.3

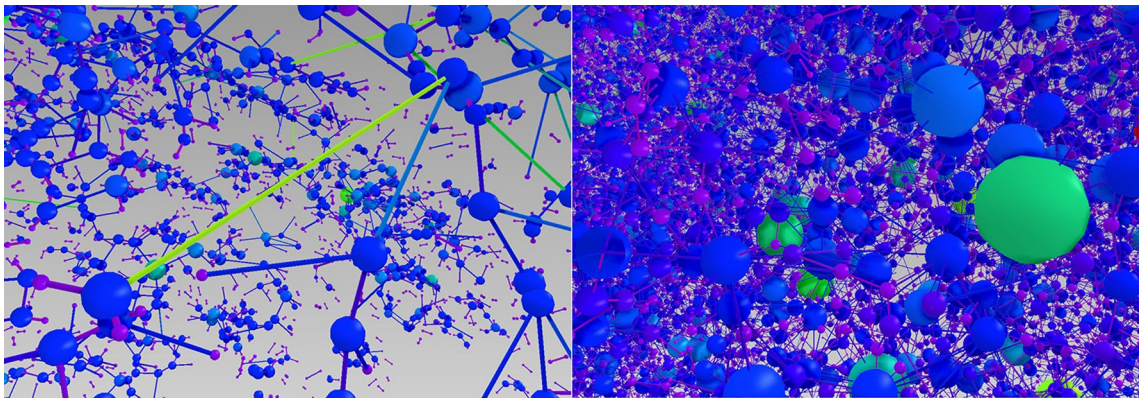

Fig. 8 Sparse graphs of pores: Left, a sample from brick A, with relatively low connectivity values and a low volume percentage of pores. Some isolated pores can be seen, along with many pores with only one or two connections. Right, a sample from brick F, with about three times higher connectivity values and volume percentage of pores. There are no isolated pores, and the system is packed very full with connected pores

Table 5 Significant ($p < .05$) data from the dense graphs of pores (Brick data = mean of 5)

Measured Variables	Brick A	Brick B	Brick C	Brick D	Brick E	Brick F
Vertex connectivity maximum	25.6	23.4	26.2	24.6	38.2	43.6
Vertex connectivity mean	2.07	2.11	2.12	2.14	2.19	2.36
Vertex connectivity SD	0.816	0.774	0.864	0.922	1.08	1.27
Vertex segment tortuosity mean	1.25	1.25	1.24	1.24	1.23	1.23
Vertex segment tortuosity SD	0.418	0.370	0.388	0.352	0.366	0.346
Vertex segment euclidean length mean µm	73.7	78.6	70.7	63.0	63.0	65.6
Vertex segment euclidean length SD µm	62.4	57.1	54.3	48.6	51.0	50.1
Edge segment tortuosity mean	1.29	1.28	1.27	1.27	1.26	1.24
Edge segment tortuosity SD	0.422	0.370	0.388	0.348	0.364	0.334
Edge segment euclidean length SD µm	51.4	45.4	37.1	36.3	39.1	37.6

to the pore system. Here the connections are removed, pores are sized and color-coded by diameter, and the black spheres are quartz sand grains that are sized by volume. For brick A, the largest sand grains tend to be near the largest (red) pores; the smallest ones tend to be on the interior within the area of the smallest (purple) pores. For brick F, which has more very large sand grains and pores, the largest sand grains are in fact touching large pores, and some large pores are in contact with multiple grains. As clay tends to pull away from large non-plastic particles during drying and firing, it makes sense that large particles might initiate the formation of large pores.

While this work is focusing on characterizing porosity and pore systems, the amount of porosity and the size, morphology, and structure of pore systems are strongly dependent on the natural and added particles present [11].

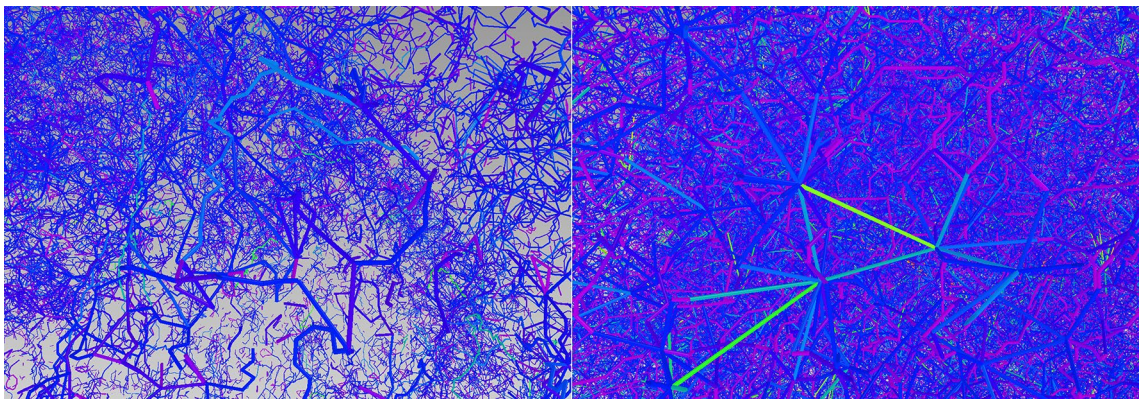

Fig. 9 Dense graphs of pores. Left, a sample from brick A, with a relatively high tortuosity. Many of the connections are twisting and taking a convoluted rather than direct path. Right, the sample from brick F, with lower tortuosity, has more connections that take a direct straight line between pores

Table 6 Significant ($p < .05$) pore network modeling variables from OpenPNM graphs of pores

Measured Variables	Brick A	Brick B	Brick C	Brick D	Brick E	Brick F
Number of vertices (pores)	4,835	2,703	4,015	4,012	3,057	1,561
Number of edges (throats)	25,683	12,877	21,030	22,496	16,180	6,564
Ratio of number of throats/number of pores	5.46	4.80	5.22	5.38	5.32	4.16
Edge direct length mean µm	416	504	442	516	505	701
Edge direct length SD µm	287	403	319	365	365	477
Edge equivalent diameter mean µm	124	125	121	137	141	155
Vertex equivalent diameter mean µm	242	241	237	257	259	278
Vertex equivalent diameter SD µm	170	236	190	216	215	292

Each entry is the means of 5 brick samples

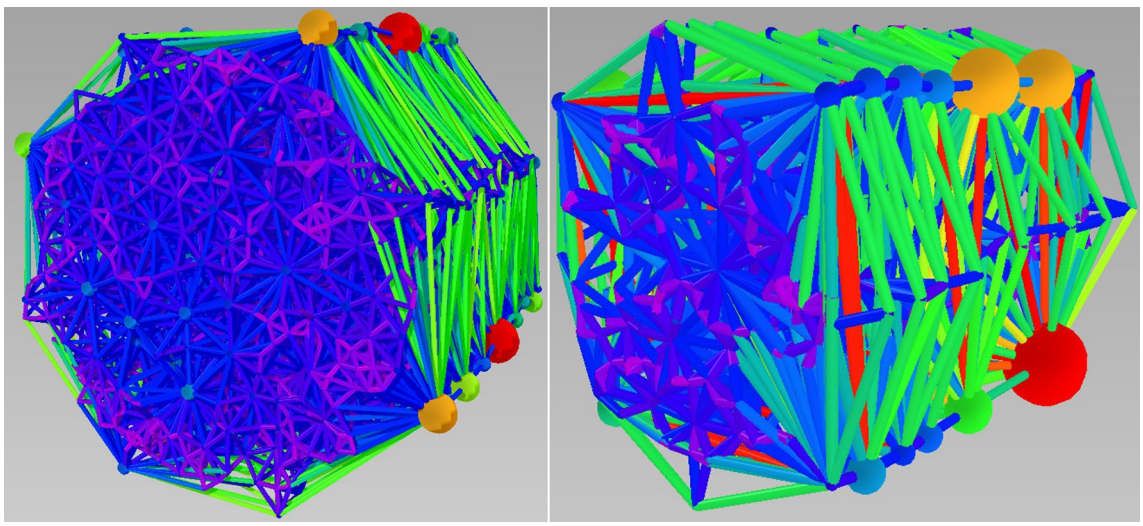

Fig. 10 Pore network models from OpenPNM, with connections sized and color-coded by direct length and pores by equivalent diameter. Left, a sample from brick A with many shorter connections between pores (purple and dark blue). Right, a sample from brick F with more longer connections (light blue, green, yellow, orange, and red) and higher equivalent diameter of connections and pores

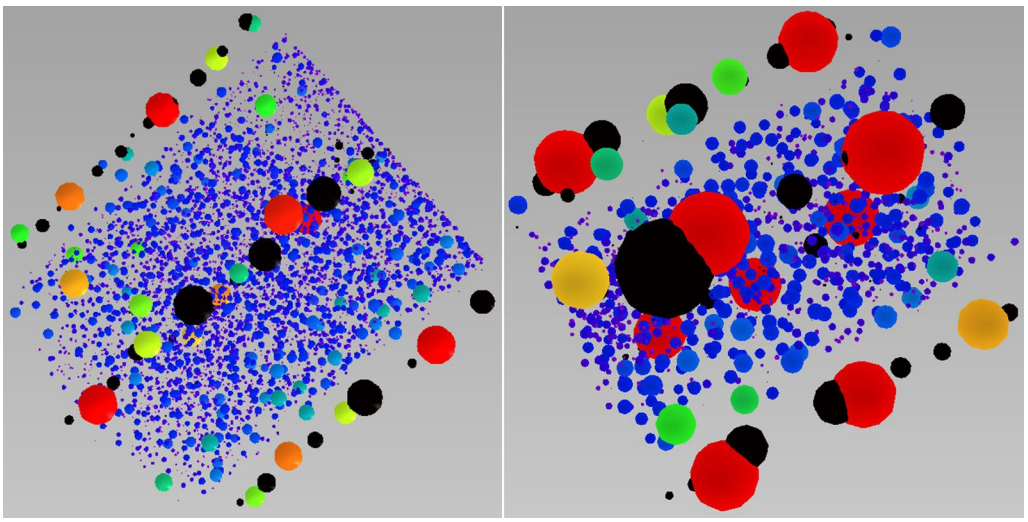

Fig. 11 Pore network models from OpenPNM superimposed with OpenPNM models of particles. Black spheres are quartz sand grains sized by volume, pore connections are removed, and pores are color-coded by diameter (from small to large: purple, dark blue, light blue, green, yellow, orange, red). Left, a sample from brick A. Right, a sample from brick F with more very large sand grains and pores; often large grains and pores are touching, with some large pores in contact with multiple grains

Additional statistical analyses

As discussed above, ANOVA identified the variables that are statistically significant in characterizing brick types and distinguishing them from other brick types in the face of the internal variation within each brick and similarities between bricks. Subsequently, those significant values were used for a stepwise linear and then quadratic discriminant analysis checked with repeated stratified k-fold cross validations to identify the combination of variables that can best discriminate between bricks. The stepwise linear discriminant analysis procedure found a combination of five variables best for predicting brick type (accuracy level of 64.4%, or an average of 19/30 samples):

(1) Volume percentage pores accessible to the surface
(2) Pore system dense graph edge scalar values segment tortuosity standard deviation
(3) Pore system sparse graph connectivity standard deviation
(4) Pore system dense graph vertex scalar values connectivity standard deviation
(5) Pore system dense graph vertex scalar values connectivity mean

The last three variables are highly correlated with each other, which is unsurprising since they all relate to pore connectivity. With only the first three pulled into the discriminant analysis, accuracy was still about 60% (an average of 18/30 samples). The best quadratic discriminant analysis was less accurate. While this is only an exploratory screening study, and the discriminant analysis results are not strong enough to rely on heavily in the conclusions, they do suggest that some specific parameters related to brick properties may be especially useful to continue examining in future studies. The volume percentage of pores accessible to the surface (versus inaccessible interior pores) is likely to have an impact on durability of a brick, since more surface-accessible pores creates more opportunities for ingress of water, salts, and pollutants. Tortuoisity is a measure of directness of connections between pores. Here the standard deviation was the best discriminator – the spread of values from those representing twisting and convoluted connections versus those representing a direct straight line between pores. Differences between bricks in this variable can create differences in the properties of permeability and diffusion. The final three discriminating variables, which are all strongly correlated with each other, indicate connectivity (number of other pores that each pore is connected to), which can impact some important functional properties of a brick such as permeability, thermal conductivity, and mechanical strength.

Conclusions

The primary conclusions are related to the original goals of this research: (1) to identify procedures for creating optimal images of pores in bricks using HR micro-CT; (2) to develop protocols for 3D image analysis to illustrate significant qualities of brick pores and to obtain

quantitative data on those pores; and (3) to clarify how HR micro-CT and the accompanying 3D image analysis data can benefit the study of porosity in historic bricks by identifying which research questions can best be addressed by this approach, the kinds of information that can be obtained, and how these analyses can best supplement other analytical techniques.

Protocol recommendations based on experience gained in this exploratory study

The first crucial choice in establishing a brick micro-CT procedure was found to be the decision about the size of each sample to be scanned. Larger sizes reveal more variability and hence are more representative of the entire brick, but they bring lower spatial resolution. For our primary instrument, we concluded that best results were achieved with samples of about 0.5 cm^3 for a 5×5 mm field of view (and 10 μm spatial resolution), then including five replicates for each brick type.

While we also had access to a Rigaku Nano 3DX CT instrument with 325 nm spatial resolution possible, since that level of resolution requires sample sizes of about 1 mm, we deemed it not useful for our current purpose of characterizing the porosity of a brick. Too much would be lost in the representativeness of samples, and it would be impossible to capture the larger pores, long cracks, and large particles surrounded by pore spaces where the clay pulled away from the particle during drying and firing. This instrument might, however, have a more limited use in examining very small pores.

Experiments with using our regular instrument for analysis of larger samples (1 cm^3 with 20 μm spatial resolution, and 2.5 cm^3 with 50 μm spatial resolution) were not satisfactory for porosity characterization. It was more difficult to segment many of the pores at those lower spatial resolutions. These resolution and segmentation problems led to more variable results.

We were also able to conduct experiments on 0.5 cm-diameter samples scanned on a Rigaku CT laboratory HX130 instrument with better spatial resolution (2.13 μm voxel size). These experiments produced excellent scans, improving the visibility of pores for segmentation. This would perhaps be a direction to go in for future studies for the quality of resulting scans. However, the computing power needed for image analysis of these higher resolution scans is an issue for consideration. With our usual instrument and 10 μm spatial resolution, the deep learning process to create a new model, using the entire scan dimensions, required about 2.5 h; then full segmentation of all slices required about five minutes. It was therefore practical to try out multiple existing models on a scan to see if any already-created ones worked well. In contrast, with the higher-resolution scans from the HX130 instrument, our computer was not powerful enough to do deep learning on the entire scan. Instead, a smaller file had to be created of a portion of the original scan. Subsequently applying a segmentation model on the entire region of interest of the scan required seven hours versus the previous five minutes. Displaying the entire scan as a multi-ROI mesh also proved to be impossible due to computer memory issues, so only part of the processed scan could be viewed. File sizes were about 0.3 GB for our usual scans but about 27.5 GB for the higher-resolution scans. To use these larger files for deep learning, segmentation, and the full 3D image processing protocols requires investment in greatly increased computing power for the laboratory (or obtaining access to high-performance computing facilities).

The next crucial choice in a micro-CT procedure for characterizing pores in a historic brick is to include sufficient replication to account for the high amount of variation typically found within a single brick, especially given the need for smaller samples to attain better spatial resolution. Yet, the literature indicates this is usually not done. We used five replicates for each brick, based on observations in the preliminary experimentation phase; additional experimentation could look at whether more replicates might be useful. Before one can compare multiple bricks, it is important to ensure that the full range of variation within each individual brick has been captured.

The Dragonfly 3D image analysis software performed well for these experiments. Other software packages would likely work as well, but since this one served our needs and is free for academic or non-profit users, we did not experiment with others. Nor did we need to spend time developing in-house image analysis algorithms since these are already available. Gaining expertise on all aspects of the image analysis package we wanted to use was a time-consuming task, so we did not expend time learning and experimenting with multiple software packages. The ability to do intensity calibration on all images with this software, bringing each image closer to the intensity values of a standard, helped reduce the number of segmentation models needed. Given the range of intensities of our samples, a single segmentation model did not work for all samples. However, the intensity calibration procedure did reduce the number of deep learning models needed to a total of nine for the 30 samples, saving considerable time (since the deep learning process required about 2.5 h/sample, about 52.5 h were saved by being able to use an existing segmentation model on 21 of the samples).

Creating segmentation models with the Dragonfly software was highly successful. Earlier in the experimentation process, when we tried to use only simple thresholding, the complexity of the samples prevented clear separation

of the matrix, pores, and particles. In contrast, results were greatly improved by using the software's capability of adding both machine learning decision trees such as Random Forest algorithms and deep learning models with convolutional neural networks using Nvidia Tensorflow to accelerate the modeling. We were able to start with an initial simple Otsu thresholding and then manually edit the results with a paint tool as a fast approach to creating dense training data. There is a library of machine learning and deep learning models available within Dragonfly to select for training, or one can create a model or import one developed on a similar sample. At each stage of training, one can predict how each model will perform on a new slice, then promote and manually edit the best-performing one. By the third slice, we usually did not need to do any further editing and the model was ready to apply to all slices of the sample.

However, the segmentation process was never "easy". The main challenge is that one must visually decide where the boundaries are between pores and ceramic matrix, and hence whether the segmentation is correct. If we had only been interested in the larger pores, there would have been little challenge, since those were obviously and consistently visually different from the matrix. However, since we were attempting to segment pores down to the limits of our spatial resolution, the decision about what to consider pores and what to consider matrix was often difficult. It has been well-documented that segmentation always has some inherent error because it is based on human perception of the difference in appearance between pores and matrix, and it can also be affected by the presence of noise and other imaging effects [38]. However, the many recent advances in image analysis algorithms and approaches have also been recognized. Nickerson et al. [52] noted that machine learning approaches improve the reliability and accuracy of segmentation of pores from solids, especially for noisy areas and edges of images. Our assessment is that a larger advantage of machine learning and deep learning approaches is the ability to segment one area or slice and then train the model on that data, then keep training and improving the model so that ultimately it can be applied to all slices of the micro-CT image. Judging the segmentation success will always be a matter of visual assessment of the accuracy of segmentation choices.

Having thin sections and enhanced images available to compare with the original raw image being used for segmentation helped in making the initial decisions about where to delineate pore boundaries. After experimenting with many image filters and filter combinations, we found that the best results for our samples came from a sequence of three image filters—gradient-domain fusion, histogram balance, and a median filter. Even better was applying the Noise2Noise regression denoising model, using deep learning to clean up noise on the original image using a copy of the image itself [51], available within our software package. Comparing these images to the original helped in making the decisions about segmentation boundaries.

Earlier in the project, we segmented all 30 samples using the scans that had been processed with the image filters, thinking those would be easier to segment. Afterwards, we learned that imaging experts do not recommend using processed images for segmentation (although that is often reported in the cultural heritage literature). We redid the analyses with the raw images, this time using the filtered ones only as an aid for making segmentation decisions. This second round of analyses, using the raw images, was indeed better—there was less variation in results for replicates within each brick type, leading to more variables being significant (in the first round of analyses with filtered images, only 12 pore variables were significant at $p < 0.05$, whereas in the second round with raw images, 41 were).

Being able to perform a variety of different 3D image analysis procedures within one software package was quite useful. Most existing micro-CT studies of brick pores include only total volume porosity and a variety of statistical properties of pore multi-ROIs related to the size and shape of pores. However, we found that the pore variables that proved to be significant came from many types of measurements and permutations on image analysis: the calculation of total volume percent of the region of interest occupied by pores, the calculation of the percentage of those pores that were accessible to the surface versus interior pores inaccessible to the surface (which requires having samples with an outer surface), calculation of statistical properties of pore multi-ROIs relating to pore size and morphology variables, connectivity data from sparse graphs of pores, data from dense graphs of pores (connectivity of pores and the length and tortuosity of connections), and data from pore network modeling using the OpenPNM plug-in available within the software (number and diameter of pores and number, length, and diameter of connections).

Porosity characterization conclusions

Multiple measures of pore size and shape were significant. This is not surprising because pore size and shape are difficult to ascertain with single measurements, given that pores are usually irregular and part of an interconnected network [16, 60]. The ANOVA was crucial in determining which of the many variables recorded were in fact significant in characterizing and distinguishing between bricks, given the variability within each brick.

The inclusion of variables related to pore connectivity, a measure of the complexity of the pore structure and related to the number of independent paths between two points within the pore space [61], proved to be important in characterizing bricks. For example, brick F had a considerably lower number of unconnected pores compared to the other bricks (with bricks A-E having a mean percentage of unconnected pores ranging from 2.4 to 3.0%, while the mean of brick F was 0.3%). Since brick F may have been made on-site at a farm using a home-constructed kiln with lower and more variable temperatures than the other bricks, which were likely made at a factory with a permanent/professional kiln, this may be an indicator of a different firing regime.

The coordination number/connectivity (number of pore throats to which each pore is connected); the number of isolated, unconnected pores; and the length, equivalent diameter, and tortuosity (shortest path analysis) of connections were obtained through the sparse and dense graphs of pores and with the pore network modeling plug-in. In addition to characterizing bricks, these variables can be used to study deterioration mechanisms. For example, large pores give a material higher permeability [55]; more connected versus unconnected pores, regardless of total porosity, creates a material that is more prone to deterioration and less durable to weathering [62]. All these variables are significant factors in flow modeling [54], and so are useful in understanding how water might be transported through and affect bricks.

While initially, we had been planning to compare porosity data from thin-section petrography to micro-CT data, it became clear early in the project that such a comparison would not be very useful. A single slice through the material, even if it is longer and wider than the micro-CT images and provides a higher magnification, cannot reproduce the volume percentages, size, shape, and connectivity data available in 3D analysis of the 3D brick materials. In fact, we found that image analysis (using the same Dragonfly software) of a single 2D thin section was often measured at about half of the total volume porosity of a micro-CT scan from the same brick. However, the thin sections were extremely helpful in making segmentation decisions, especially about particles, and would be especially helpful in projects where particles were a major focus since the thin section data can be used to help distinguish between particle types in the micro-CT scans (where particles of similar density to each other and to the matrix can be difficult to discern for segmentation). Thin section petrography is also crucial for identifying the minerals, lithics, and organic particles present, whereas micro-CT scans are of limited use for that purpose.

While we expected to find an increase in porosity with the accelerated weathering of samples, in the three samples of modern hand-molded bricks studied, only one sample did show a porosity increase. To examine this issue further would require additional replication; it is likely that a longer period of accelerated aging is needed, including adding multiple freeze–thaw cycles. If increased porosity continues to be found, then it may be useful to look at other parameters such as surface-accessible/inaccessible interior pore ratios and connectivity changes resulting from weathering, so this will be a focus of future work.

This project identified a set of protocols for creating good working images of pores in bricks in micro-CT scans. It also provided a detailed set of protocols for performing 3D image analysis of those scans for qualitative and quantitative data and for identifying which variables are statistically significant in characterizing bricks. A variety of types of pore data were found to be potentially important for characterizing bricks through micro-CT and 3D image analysis. These data can also potentially be used to identify bricks that may be more susceptible to weathering and deterioration due to pore structures and systems that better enable movement of water into and throughout the brick. Future research will focus on the addition of selected nano-CT measurements to assess the population of very small pores that are missed due to the spatial resolution of micro-CT [9], expanded studies of the effects of accelerated weathering on brick pore systems, and use of the software on a high-performance supercomputer cluster to enable faster image analysis of micro-CT scans of higher spatial resolution that are difficult to analyze on a laboratory computer.

Abbreviations

HR micro-CT: High-resolution micro-computed tomography; 3D: Three-dimensional; MIP: Mercury intrusion porosimetry.

Acknowledgements

The HR micro-CT equipment was made available by the Advanced Materials Characterization Laboratory at the University of Delaware. The authors gratefully acknowledge the laboratory's facility manager, Gerald Poirier, for his assistance in developing a micro-CT analysis plan, and to Aya Takase at Rigaku for sharing her micro-CT expertise and providing comparative analyses on a Rigaku HX130 instrument. Thanks are due to Mike Marsh at Object Research Systems for his "Daily Dragonfly Webinars" which greatly helped in the design of this project's 3D image analysis protocols. We also acknowledge Zixong Cao at Object Research Systems for additional advice in the use of the Dragonfly software. Dr. Terry J. Reedy assisted in the brick sampling design and in the design of the data tables. Steve S. Martin and Michael J. Emmons, Jr. provided historic bricks for this research.

Author contributions

ChLR designed the experiments, was the main contributor in writing the manuscript, and carried out the micro-CT work, 3D image analysis, and thin-section petrography. CLR was responsible for the statistical analyses and their interpretations. Both authors read and approved the final manuscript.

Funding
The research reported here was funded by the U.S. National Park Service, National Center for Preservation Technology and Training, under grant number P19AP00143.

Availability of data and materials
The datasets used and/or analyzed during the current study are available from the corresponding author on reasonable request.

Declarations

Competing interests
The authors declare that they have no competing interests.

Author details
[1]Center for Historic Architecture and Design, University of Delaware, 240 Academy Street, 331 Alison Hall, Newark, DE 19716, USA. [2]Biomedical Research Informatics Center, Nemours Children's Hospital, Wilmington, DE 19803, USA.

Received: 20 January 2022 Accepted: 30 May 2022
Published online: 13 June 2022

References

1. Anovitz LM, Cole DR. Characterization and analysis of porosity and pore structures. Rev Mineral Geochem. 2015;80:61–164.
2. Abell AB, Willis KL, Lange DA. Mercury intrusion porosimetry and image analysis of cement-based materials. J Colloid Interface Sci. 1998;211:39–44.
3. Cultrone G, Sebastián E, Elert K, de la Torre MJ, Cazalla O, Rodriguez-Navarro C. Influence of mineralogy and firing temperature on the porosity of bricks. J Eur Ceram Soc. 2004;24:547–64.
4. Little JE, Yuan X, Jones MI. Characterization of voids in fibre reinforced composite materials. NDT&E Inter. 2012;46:122–7.
5. Rouquerol J, Baron GV, Denoyel R, Giesche H, Groen J, Klobers P, Levitz P, Neimark AV, Rigby S, Skudas R, Sing K, Thommes M, Unger K. The characterization of microporous solids: an overview of methodology. Microporous Mesoporous Mater. 2012;154:2–6.
6. Sobott R, Bente K, Kittel M. Comparative porosity measurements on ceramic materials. Old Potter's Alm. 2014;19:18–25.
7. Ricci G, Kulkov AM, Kulkova MA, Zendri E. Experimental analyses by X-ray μ-CT for the study of the effects of firing temperature on the ceramic body morphology. Brussels: Bruker Micro-CT User Meeting; 2017. p. 168–71.
8. Cai T, Feng Z, Zhou D. Multi-scale characteristics of coal structure by X-ray computed tomography (X-ray CT), scanning electron microscope (SEM) and mercury intrusion porosimetry (MIP). AIP Adv. 2018;8: 025324.
9. Puskarczyk E, Krakowska P, Jędrychowski M, Habrat M, Madejski P. A novel approach to the quantitative interpretation of petrophysical parameters using nano-CT: example of Paleozoic carbonates. Acta Geophys. 2018;66:1453–61.
10. Chen F, Lu S, Ding X, Zhao H, Ju Y. Total porosity measured for shale gas reservoir samples: a case from the Lower Silurian Longmaxi Formation in southeast Chongqing. China Minerals. 2019;9:5.
11. Buchner T, Kiefer T, Zelya-Lainez L, Gaggi W, Konegger T. A multitechnique, quantitative characterization of the pore space of fired bricks made of five clayey raw materials used in European brick industry. Appl Clay Sci. 2021;200: 105884.
12. Wang C, Hua Y, Nadimi S, Taleb W, Barker R, Li Y, Chen X, Neville A. Determination of thickness and air-void distribution within the iron carbonate layers using X-ray computed tomography. Corros Sci. 2021;179: 109153.
13. Coletti C, Cultrone G, Maritan L, Mazzoli C. Combined multi-analytical approach for study of pore system in bricks: how much porosity is there? Mater Charact. 2016;121:82–92.
14. Bugani S, Camaiti M, Morselli L, Van de Casteele E, Janssens K. Investigation on porosity changes of Lecce stone due to conservation treatments by means of X-ray nano- and improved micro-computed tomography: preliminary results. X-ray Spectrom. 2007;36:316–20.
15. Stefanidou MA. Assimilation of porosity in modern bricks by computational means. WIT Trans Eng Sci. 2007;57:313–8.
16. Klobes P, Meyer K, Munro RG. Porosity and specific surface area measurements for solid materials. Washington, DC: National Institute of Standards and Technology; 2006.
17. Kilikoglou V, Vekinis G, Maniatis Y. Toughening of ceramic earthenwares by quartz inclusions: an ancient art revisited. Acta Metal Mater. 1995;43:2959–65.
18. Kilikoglou V, Vekinis G, Maniatis Y, Day PM. Mechanical performance of quartz-tempered ceramics: part 1, strength and toughness. Archaeometry. 1998;40:261–79.
19. Reedy CL. Thin section petrography of stone and ceramic cultural materials. London: Archetype Publications; 2008.
20. Quinn PS. Ceramic petrography. London: Archaeopress; 2013.
21. Rice PM. Pottery analysis: a sourcebook. Chicago and London: University of Chicago Press; 2015.
22. Kahl W-A, Ramminger B. Non-destructive fabric analysis of prehistoric pottery using high-resolution X-ray microtomography: a pilot study on the late Mesolithic to Neolithic site Hamburg-Boberg. J Archaeol Sci. 2012;39:2206–19.
23. Park KS, Milke R, Rybacki E, Reinhold S. Application of image analysis for the identification of prehistoric ceramic production technologies in the North Caucasus (Russia, Bronze/Iron Age). Heritage. 2019;2:2327–42.
24. Reedy CL, Anderson J, Reedy TJ. Quantitative porosity studies of archaeological ceramics by petrographic image analysis. Mat Res Soc Symp Proc. 2017;1656:337–53.
25. Grubeša IN, Vračevič M, Ducman V, Marković B, Szenti I, Kukovecz Á. Influence of the size and type of pores on brick resistance to freeze-thaw cycles. Materials. 2020;13:3717.
26. Tang Y, Shao Z, Xu T. Pore structure of ancient Chinese bricks under environmental vicissitudes. KSCE J Civ Eng. 2016;5:1895–902.
27. Borelli E. Porosity. Rome: ICCROM; 1999.
28. Gavilán ABR, Esteban MAR, Iglesias MNA, Perez MPS, Olea MSC, Valdizán JC. Experimental study of the mechanical behaviour of bricks from 19th and 20th century buildings in the province of Zamora (Spain). Infrastructures. 2018;3:38.
29. Torraca G. Porous building materials. Rome: ICCROM; 2005.
30. Chen X. Performance simulation of brick construction under the impacts of increased precipitation as a consequence of climate change. University of Pennsylvania: MA Thesis 2018.
31. Delbrouck O, Janssen J, Ottenburgs R, Van Oyen P, Viaene W. Evolution of porosity in extruded stoneware as a function of firing temperature. Appl Clay Sci. 1993;8:187–92.
32. Studart AR, Gonzenback UT, Tervoort E, Gauckler LJ. Processing routes to microporous ceramics: a review. J Am Ceram Soc. 2006;89:1771–89.
33. Orts MJ, Escardino A, Amorós JL, Negre F. Microstructural changes during the firing of stoneware floor tiles. Appl Clay Sci. 1993;8:193–225.
34. Kariem H, Hellmich C, Kiefer T, Jäger A, Füssi J. Micro-CT-based identification of double porosity in fired clay objects. J Mater Sci. 2018;53:9411–28.
35. Copley DC, Eberhardt JW, Mohr GA. Computed tomography part I: Introduction and industrial applications. JOM. 1994;46:14–26.
36. Goldman LW. Principles of CT and CT technology. JNMT. 2007;35:115–28.
37. Wilson PF, Smith MP, Hay J, Warnett JM, Attridge A, Williams MA. X-ray computed tomography (XCT) and chemical analysis (EDX and XRF) used in conjunction for cultural conservation: the case of the earliest scientifically described dinosaur *Megalosaurus bucklandii*. Herit Sci. 2018;6:58.
38. Cnudde V, Boone MN. High-resolution X-ray computed tomography in geosciences: a review of the current technology and applications. Earth Sci Rev. 2013;123:1–17.
39. Rueckel J, Stockmar M, Pfeiffer F, Herzen J. Spatial resolution characterization of a microCT system. Appl Radiat Isot. 2014;94:230–4.
40. Dunsmuir JH, Vandiver PB, Chianelli RR, Deckman HW, Hardenbergh JH. X-ray microtomography of ceramic artifacts. Mat Res Soc Symp Proc. 1995;352:73–83.
41. Cnudde V, Masschaele B, Dierick M, Vlassenbroeck J, Van Hoorebeke L, Jacobs P. Recent progress in X-ray CT as a geosciences tool. Appl Geochem. 2006;21:826–32.
42. Pearce JK, Golab A, Dawson GKW, Knuefing L, Goodwin C, Golding SD. Mineralogical controls on porosity and water chemistry during

O_2-SO_2-CO_2 reaction of CO_2 storage reservoir and cap-rock core. Appl Geochem. 2016;75:152–68.
43. Du Plessis A, Babatunde JO, Boshoff WP, le Roux SG. Simple and fast porosity analysis of concrete using X-ray computed tomography. Mater Struct. 2016;49:553–62.
44. Porter ML, Wildenschild D. Image analysis algorithms for estimating porous media multiphase flow variables for computer tomography data: a validation study. Comput Geosci. 2010;14:15–30.
45. Maynard, WB. New Castle's Dutch Tile House of 1687: Fraud or genuine? Delaware History. 2001;29:141-68. This is a semi-annual journal publication of the Delaware Historical Society in Wilmington, DE. ISSN: 0011-7765 https://dehistory.org/learn/publications/
46. Robinson GC. Characterization of bricks and their resistance to deterioration mechanisms. In: Shellenbarger M, editor. Conservation of historic stone buildings and monuments. Washington DC: National Academies Press; 1982. p. 147–61.
47. Everett DH. International union of pure and applied chemistry, division of physical chemistry. Manual of symbols and terminology for physicochemical quantities and units. Appendix II: Definitions, terminology and symbols in colloid and surface chemistry, part 1. Pure Appl Chem. 1972;31:579–638.
48. Cantrell DL, Hagerty RM. Microporosity in Arab Formation carbonates, Saudia Arabia. Geoarabia. 1999;4:129–54.
49. Object Research Systems. https://www.theobjects.com/company/index.html. Accessed 14 April 2022.
50. Otsu N. A threshold selection method from gray-level histograms. IEEE Trans Man Cybern. 1979;9:62–6.
51. Lehtinen J, Munkberg J, Hasselgren J, Laine S, Karras T, Aitala M, Aila T. Noise2Noise: learning image restoration without clean data. Proc ICML. 2018. https://doi.org/10.48550/arXiv.1803.04189.
52. Nickerson S, Shu Y, Zhong D, Könke C, Tandia A. Permeability of porous ceramics by X-ray CT image analysis. Acta Mater. 2019;172:121–30.
53. Gostick J, Aghighi M, Hinebaugh J, Tranter T, Hoeh MA, Day H, Spellacy B, Sharqawy MH, Bazylak A, Burns A, Lehnert W, Putz A. OpenPNM: a pore network modeling package. Comput Sci Eng. 2016;18(4):60–74.
54. Munawar MJ, Lin C, Cnudde V, Bultreys T, Dong C, Zhang X, De Boever W, Zahid MA. Petrographic characterization to build an accurate rock model using micro-CT: case study on low-permeable to tight turbidity sandstone from Eocene Shahejie formation. Micron. 2018;109:22–33.
55. Thomson P-R, Aituar-Zhakupova A, Hier-Majumder S. Image segmentation and analysis of pore network geometry in two natural sandstones. Front Earth Sci. 2018. https://doi.org/10.3389/feart.2018.00058.
56. Spectrum Petrographics. http://www.petrography.com/. Accessed 14 April 2022.
57. Layman II JM. Porosity characterization utilizing petrographic image analysis: Implications for identifying and ranking reservoir flow units, Happy Spraberry Field, Garza County, Texas. Texas A&M University: MS Thesis; 2002.
58. Dicus CM. Relationship between pore geometry, measured by petrographic image analysis, and pore-throat geometry, calculated from capillary pressure, as a means to predict reservoir performance in secondary recovery programs for carbonate reservoirs. Texas A&M University: MA Thesis; 2007.
59. De Graef B, Cnudde V, Dick J, De Belie N, Jacobs P, Verstraete W. A sensitivity study for the visualisation of bacterial weathering of concrete and stone with computerised X-ray microtomography (CT). Sci Total Environ. 2005;341:173–83.
60. Haruzi P, Katsman R, Halisch M, Waldmann N, Spiron B. Benchmark study using a multi-scale, multi-methodological approach for the petrophysical characterization of reservoir sandstones. Solid Earth. 2021;12:665–89.
61. Pierret A, Capowiez Y, Belzunces L, Moran CJ. 3D reconstruction and quantification of macropores using X-ray computed tomography and image analysis. Geoderma. 2002;106:247–71.
62. López-Arce P, Zornoza-Indart A, Gomez-Villalba L, Pérez-Monserrat EM, Alvarez de Guergo M, Vivar G, Fort R. Archaeological ceramic amphorae from underwater marine environments: influence of firing temperature of salt crystallization decay. J Eur Ceram Soc. 2013;33:2031–42.

Publisher's Note

Springer Nature remains neutral with regard to jurisdictional claims in published maps and institutional affiliations.

Submit your manuscript to a SpringerOpen journal and benefit from:

- ► Convenient online submission
- ► Rigorous peer review
- ► Open access: articles freely available online
- ► High visibility within the field
- ► Retaining the copyright to your article

Submit your next manuscript at ► springeropen.com